Article

Uncovering a widely applicable empirical formula for field emission characteristics of metallic nanotips in nanogaps

Check for updates

Yimeng Li [1], Linghan Xia[1], Nan Li[1], Shilong Tang[1], Yunsong Ge[1], Jianyu Wang[1], Bing Xiao[1], Yonghong Cheng[1], Lay Kee Ang [2] ✉ & Guodong Meng [1] ✉

Field electron emission is a key mechanism in nanoelectronics with nanogaps, offering advantages such as high electron velocity and fast switching speeds. However, nanoscale field emission, affected by geometric asymmetry including quantum tunneling near to the emitter, and quantum space charge effects, remains largely unexplored in experimental studies. Here, we in situ investigated field emission characteristics of pure tungsten nanotips across vacuum nanogaps. We revealed a widely applicable scaling behavior between field emission characteristics and the ratio of apex radius to gap length (R/d), and demonstrated that the effects of quantum tunnelling due to emitter shape are the predominant influence. We further proposed a modified field emission equation, incorporating an empirical formula for the apex shape factor, k_{MG} ($k_{MG} = f(R/d) = 1.680 \times (R/d + 0.468)^{-1.066}$), valid for $R/d = 0.04$ to 48. These findings provide fundamental insights into the optimization of nanoelectronic device design and the advancement of future technologies.

Tremendous efforts in development of novel nanomechanical fabrication techniques and devices have witnessed a variety of emerging nanoelectronics, including field emission diodes[1–3], field effect transistors[4–12], ultrafast switches[13–17], biosensors[18–20], and molecular transistors[21,22]. The typical device structure has a vacuum nanogap as an electron transport channel, which is expected to show extraordinary performances in terms of the high electron traveling velocity, fast switching rates, high operating temperatures, and exceptional radiation tolerance. Specially designed with asymmetric electrode structures and operating at low voltages, these devices rely heavily on field electron emission (FE)[3,6,9,17,23–25]. The state-of-the-art ultrafast nanoelectronic switches reported in *Nature* has successfully achieved picosecond-level switching speeds with lower power consumption by utilizing electron field emission induced nanoplasma[13,14]. However, 1950s type planar FE theory, based on the 1956 Murphy-Good (MG) FE equation (see Supplementary Note 1)[26–28], does not work well for nanodevices. This is because the traditional planar potential barrier, the so-called Schottky-Nordheim barrier (Supplementary Eq. (S1)), does not adequately describe the potential-energy variation near a

significantly curved surface[29,30]. Further, when the gap distance is at the nanometer scale, quantum effects may occur, particularly if there is significant space-charge in the gap[31–33]. These quantum effects are, firstly that it may become necessary to describe the electron motion in the gap by using the Schrödinger equation (rather than by using classical space-charge arguments), secondly that it may become necessary to consider exchange-and-correlation interactions between electrons in the space-charge. Both effects are difficult to clearly distinguish when the size of the emitter is comparable to the nanogap spacing.

Generally, for typical sharp emitters, it is common practice to assume that the average electrostatic field F_0 is enhanced by a field enhancement factor (FEF) of γ in Supplementary Eq. (S2): $F = \gamma F_0 = \gamma V/d$, where F is the absolute magnitude of the electrostatic field at emitter surface, and γ depends on the definition of the distance d, either as the distance between planar plates (plate FEF), particularly for a post standing on one of a pair of parallel plates, or as the distance between the emitter apex and the anode plate (gap FEF)[34,35]. However, this approach by itself may fail to accurately predict the field emission

[1]State Key Laboratory of Electrical Insulation and Power Equipment, Xi'an Jiaotong University, Xi'an, P.R. China. [2]Science, Mathematics and Technology, Singapore University of Technology and Design, Singapore, Singapore. ✉e-mail: ricky_ang@sutd.edu.sg; gdmengxjtu@xjtu.edu.cn

behavior of emitter tips with apex radii R less than 50 nm, as the width of tunneling barrier is getting very sensitive to the physical dimension[36–43]. Previous studies have reported that during field emission from nanotips, the electron total-energy distributions sometimes display multiple well-separated peaks rather than one strong peak at Femi level, indicating a considerable variation of the structure of electron states inside the nano-emitter[44,45]. Currently, most FE models proposed in the literatures for nano-emitters either are focused on the corrections of the supply function and transmission coefficient due to probable quantum confinement effects of emitter with a non-planar geometry or are mainly aimed to calculate the image charge potential of space charges with cathode alone more accurately by including the geometric effects in the related mathematical formulation[42,46–49]. It is important to note that the supply function and transmission coefficient can be strongly geometrically dependent. This complexity suggests that it is nearly impossible to have an analytical multi-dimensional field emission model for a given emitter. This has prompted this experimental attempt to obtain an empirical scaling.

Moreover, when developing a FE model for nanogaps, a sophisticated approach has been to obtain space charge limited field emitted current density by solving the coupled Schrödinger and Poisson equations self-consistently[50–54]. Therefore, the question of whether quantum effects of this kind need to be considered turns out to be a very fundamental issue for further elucidating the intrinsic and experimental field emission characteristics at the nanoscale.

Here, we studied the experimental field emission characteristics of the pure tungsten nanoelectrodes across vacuum nanogaps by utilizing a home-built in situ electrical experiment system. We explored how the field emission characteristics vary as a function of the ratio of apex radius to gap length (R/d in the range of 0.04 to 48) and revealed a consistent scaling relationship between them. This scaling is shown to recover the accepted limits at $R/d \ll 1$ (ultrasharp tip) and $R/d \gg 1$ (planar gap). Furthermore, after excluding the space charge quantum effects, we successfully proposed a modified FE equation that accounts for geometric asymmetry effects and related R/d dependence. Finally, the I-F curves and corresponding FN plots based on this FE equation are compared with previous experimental results.

Results and discussion

In situ field emission measurement at nanoscale

Experimental field emission characteristics from various nanoscopic emitters in nanogaps are tested using an in situ electrical experiment system, which comprises a transmission electron microscopy (JEOL-2100F TEM) and an in situ electrically biased TEM holder (ZepTools Technology)[55,56]. The electrode structure is tungsten nanotip (W, cathode)−gold plate (Au, anode), and the pure tungsten nanotips with different apex radii of curvature are prepared by a two-step process: the ex-situ double-electrolyte electrochemical etching method[57,58] and the in situ Joule melting method[59]. Details of the in situ electrical measurement system and the preparation of tungsten nanotips are described in the "Methods" section. In this work, we investigated the field emission characteristics of tungsten nanotips with apex radii of curvature R_m (measured from TEM images) ranging from 2 nm to 190 nm across various nanogaps (5 nm ≤ d_m ≤ 100 nm), which covers a wide range of $R_m/d_m = 0.04$ to 48. Notably, in our experiments, the gap distance d_m refers to the distance between the emitter apex and the anode plate. The TEM images of these tungsten nanotips are shown in Fig. 1.

Field emission characteristics

Figure 2a, b presents the experimental field emission I_m-V_m curves (solid lines) and the corresponding Fowler-Nordheim (FN) plots (solid lines) of the tungsten nanotip with an apex radius of 4 nm, across nanogaps d_m ranging from 5 nm to 80 nm. As depicted, the current increases rapidly as the voltage reaches the turn-on threshold, and with increasing nanogap distance, the I_m-V_m curves shift towards higher voltages. Notably, all FN plots exhibit a nearly linear relationship, indicating the typical field emission behavior. The dotted lines in Fig. 2a, b represent theoretical I_{MG}-$V_{MG\text{-}eff}$ data generated as described in the following Section. The experimental field emission I_m-V_m curves of all tungsten nanotips offer valuable insights into how both the radius of curvature R_m of nanotips and the gap spacing d_m affect their emission characteristics. Figure 2c–e illustrate the applied voltages V_m (measured at $I_m = 2$ nA), the FEFs γ_a, and the $\gamma_a \cdot V_m$ as functions of R/d in logarithmic coordinates (scatterplots). Here, γ_a is obtained from finite element method (FEM) simulations (see "Methods" section and
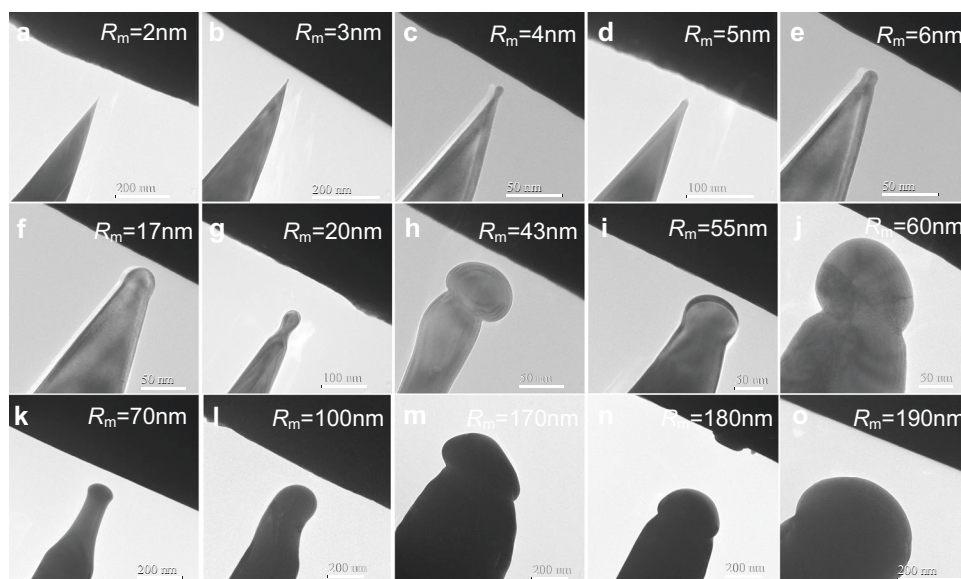

Fig. 1 | The transmission electron microscopy (TEM) images of tungsten nanotips with apex radii (R_m) ranging from 2 nm to 190 nm. a $R_m = 2$ nm. **b** $R_m = 3$ nm. **c** $R_m = 4$ nm. **d** $R_m = 5$ nm. **e** $R_m = 6$ nm. **f** $R_m = 17$ nm. **g** $R_m = 20$ nm. **h** $R_m = 43$ nm. **i** $R_m = 55$ nm. **j** $R_m = 60$ nm. **k** $R_m = 70$ nm. **l** $R_m = 100$ nm. **m** $R_m = 170$ nm. **n** $R_m = 180$ nm. **o** $R_m = 190$ nm.
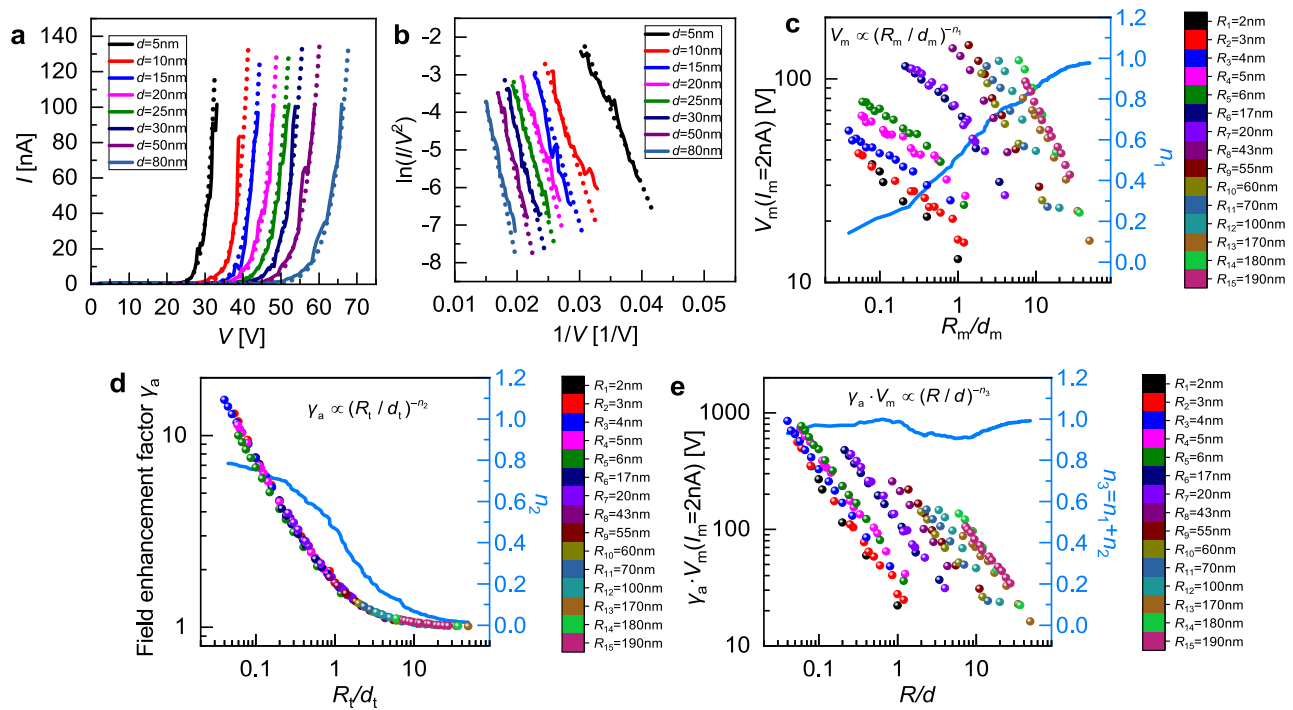
Fig. 2 | Field emission (FE) characteristics at nanoscale. a The experimental field emission current-voltage I_m-V_m curves (solid lines) of the tungsten nanotip with an apex radius of 4 nm across different nanogaps. The dotted lines represent the theoretical I_{MG}-$V_{MG\text{-eff}}$ data based on the Murphy-Good (MG) FE equation ($V_{MG\text{-eff}} = V_{MG}/C_{MG} \approx V_m$, where C_{MG} is correction factor). **b** The corresponding experimental Fowler-Nordheim (FN) plots (solid lines) and the corresponding FN plots (dotted lines) based on the MG FE equation ($V_{MG\text{-eff}} = V_{MG}/C_{MG} \approx V_m$) of the tungsten nanotip with an apex radius of 4 nm. **c** The applied voltages V_m at a field emission current (I_m) of 2 nA as a function of the ratio of experimental apex radius to gap length (R_m/d_m) in logarithmic coordinates (scatterplots), along with the corresponding negative exponent n_1 (solid line). **d** The field enhancement factors γ_a obtained from simulation as a function of simulated apex radius to gap length (R_t/d_t) in logarithmic coordinates (scatterplots), along with the corresponding negative exponent n_2 (solid line). **e** The product $\gamma_a \cdot V_m$ of the field enhancement factors γ_a and the applied voltages V_m at $I_m = 2$ nA as a function of R/d in logarithmic coordinates (scatterplots), along with the corresponding negative exponent n_3 (solid line).

Supplementary Fig. 3), where the nanotips are modeled using the sphere-on-cone approach, based on the morphology of all the tungsten nanotips in Fig. 1. Notably, although the nanotip models are constructed using parameters (R_m, d_m) measured from TEM images, they may not perfectly match the experimental nanotips. Thus, the radius of curvature of nanotip models and the gap distance in FEM simulations are denoted by R_t and d_t, to distinguish them from the experimental nanotips, even though $R_t = R_m$ and $d_t = d_m$. From the FEM electrostatics simulations, γ_a can be obtained as $\gamma_a = F_a/F_G$, where F_a represents the electrostatic surface-field magnitude at the emitter apex, and F_G is the average field amplitude in the gap between the emitter apex and the anode plate, given by $F_G = V_m/d_t$. It's important to note that our experiments are conducted in a near anode configuration, where the total emitter height $H_m \gg R_m$ and $H_m \gg d_m$, meaning that γ is not sensitive to H. To minimize the effect of the simulated height on the electrostatic fields, we set the height of the simulation models to be sufficiently large (at $H_t/R_t = 400$) as shown in the "Methods" section and Supplementary Fig. 2. The relationships $V_m \propto (R_m/d_m)^{-n_1}$, $\gamma_a \propto (R_t/d_t)^{-n_2}$, and $\gamma_a \cdot V_m \propto (R/d)^{-n_3}$ are used to obtain the fitted values of n_1, n_2, and n_3 based on R/d, respectively, as shown in Fig. 2c–e. As expected, the required applied voltages V_m (at a fixed current) and the γ_a decrease with higher values of R/d. Notably, the relationship between γ_a and R_t/d_t is nearly identical for all tungsten nanotip sphere-on-cone models with different R_t at different gap spacing d_t (Fig. 2d). For R_m/d_m values less than 0.1, n_1 increases slowly to about 0.2, rises rapidly to 0.9 as R_m/d_m approaches 10, and then increases more slowly towards 1 for R_m/d_m greater than 10, reflecting a transition to planar geometry with the relationship approximated as $V_m \propto d_m/R_m$ (Fig. 2c). Similarly, for $R_t/d_t < 0.1$, the electrostatic field distribution between the

emitter apex and the anode plane is non-uniform with n_2 decreasing slowly to about 0.8, becoming more uniform as R_t/d_t increases to 10 (where n_2 drops rapidly to about 0.1), and approaching a planar case for $R_t/d_t > 10$ with γ_a nearing 1 or $n_2 = 0$ (Fig. 2d). More importantly, for all nanotips in our experiments, n_3 is approximately 1 (Fig. 2e), with acceptable fluctuations due to the differences between the experimental nanotips and the sphere-on-cone models. Therefore, we disregard the subscript differences "m" and "t" for R and d, obtaining the following relationship: $\gamma_a \cdot V_m \propto d/R$, which further leads to $F_a = \gamma_a \cdot F_G \propto 1/R$. This finding implies that the local electrostatic field strength at the emitter apex required to obtain the same field emission current remains largely unchanged across the range of $R/d = 0.04$ to 48, with values for different nanotips depending on their apex radii of curvature. Moreover, within this range of R/d, even with a minimum R of 2 nm and d of 5 nm, no significant deviations from this relationship $\gamma_a \cdot V_m \propto d/R$ ($F_a = \gamma_a \cdot F_G \propto 1/R$) are observed in Fig. 2e. This suggests that the effects due to the non-planar shape of the emitter may play a critical role in nanoscale field emission process. Notably, these relationships hold across various field emission currents in the nanoampere (nA) range. Additional details, including the logarithmic relationship between applied voltages V_m and R_m/d_m, as well as between $\gamma_a \cdot V_m$ and R/d at different field emission currents of (10, 50, and 100 nA), are provided in Supplementary Fig. 4.

Notably, the aforementioned relationships are based on experimental data or simulated data, and the specific analytical scaling (i.e., the specific analytical relationship between $\gamma_a \cdot V_m$ and R/d has yet to be derived (which may not be possible). Generally, the electrostatic field at the emitter apex can be expressed as $F_a = \beta_a \cdot V_m = V_m/(k_a R)$, where β_a is the conversion factor connecting the electrostatic surface-field
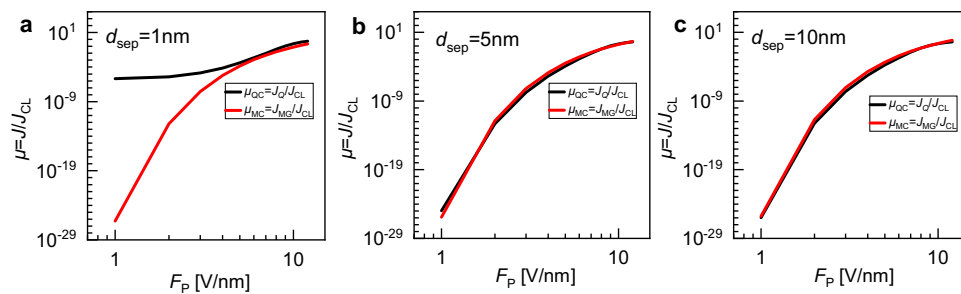
Fig. 3 | The theoretical normalized electron emission current density in nanogaps. a The normalized electron emission current density $\mu_{QC} = J_Q/J_{CL}$ (black lines) and $\mu_{MC} = J_{MG}/J_{CL}$ (red lines) as a function of electrostatic fields $F_P = 1$ to 12 V/nm ($F_P = V_P/d_{sep}$, V_P is the applied voltage between the plates) at $d_{sep} = 1$ nm for the tungsten (cathode)-gold (anode) parallel-plate electrode structure, based on theoretical calculations. Here, J_{CL} is the classical Child-Langmuir (CL) law, J_{MG} is the MG FE equation, and J_Q is obtained by a self-consistent quantum model[53,54]. **b** $\mu_{QC} = J_Q/J_{CL}$ (black lines) and $\mu_{MC} = J_{MG}/J_{CL}$ (red lines) at $d_{sep} = 5$ nm. **c** $\mu_{QC} = J_Q/J_{CL}$ (black lines) and $\mu_{MC} = J_{MG}/J_{CL}$ (red lines) at $d_{sep} = 10$ nm.

magnitude at the emitter apex and the applied voltages, and k_a is a shape factor to be determined either experimentally or numerically[60]. The previous theoretical analytical scaling[60] at the apex of the microtip with the prolate-spheroidal shape (which also used the assumption in Supplementary Note 1) shows $k_a = 0.5 \times \ln(4\,d/R)$ and $k_a = d/R$, respectively, for $R/d \ll 1$ (sharp tip) and $R/d \gg 1$ (planar limit). By writing $F_a = \beta_a \cdot d \cdot V_m/d = \gamma_a \cdot F_G$, we have $\gamma_a = \beta_a \cdot d = d/(k_a R)$, which gives $\gamma_a = 2/(R/d)$ and $\gamma_a = 1$ (see the derivation in Supplementary Note 2), respectively, for $R/d \ll 1$ (sharp tip) and $R/d \gg 1$ (planar limit), which is consistent with results shown in Fig. 2d. It is important to note that the geometrical shape of our experimental tip (in Fig. 1) is not exact similar to the assumed in ref. 60, but the discussion above shows qualitative agreement.

Geometric effects at nanoscale

To further determine whether the space charge quantum effects are significant in our experiment, we used a self-consistent quantum model, which has been reported in refs. 53,54, to obtain the field emission characteristics J_Q for the tungsten (cathode)-gold (anode) parallel-plate electrode structure[50–54]. In this model, the one-dimensional modified Poisson-Schrödinger equation combined with the Jeffreys-Wentzel-Kramers-Brillouin tunneling model is solved numerically for calculating electron field emission current density[54]. The local work function (ϕ) and Fermi Energy (E_F) used for tungsten are given as 4.5 eV and 5.782 eV, respectively, and for gold, they are 5.1 eV and 5.535 eV, respectively[61]. Figure 3 shows the normalized electron current density $\mu_{QC} = J_Q/J_{CL}$ (black lines) compared to $\mu_{MC} = J_{MG}/J_{CL}$ (red lines) at different distances between well-separated parallel planar plates ($d_{sep} = 1$ nm, 5 nm, and 10 nm) based on theoretical calculations, where J_{CL} is the classical Child-Langmuir (CL) law[62,63], and the J_{MG} is the MG FE equation without the space charge effects (see Supplementary Note 1 and Supplementary Eq. (S2)). When the gap distance d_{sep} is greater than 5 nm and the electrostatic field F_P ($F_P = V_P/d_{sep}$, V_P is the applied voltage between the plates) is less than 10 V/nm, the field emission characteristics considering space charge quantum effects are consistent with those obtained by MG FE equation. This indicates that the space charge quantum effects can be ignored so that we can conclude the effects due to the non-planar shape of the emitter are more important for $R/d = 0.04$ to 48 as studied in our experiment. Moreover, it should be noted that when d_{sep} is 1 nm and F_P is less than 4 V/nm, the emission current density μ_{QC} is higher than μ_{MC}, due to direct tunneling (see Supplementary Note 3 and Supplementary Fig. 5)[54].

Since the space charge quantum effects can be ignored in our experiment, we further compare the experimental current-voltage I_m-V_m characteristics with theoretically predicted characteristics. The representative geometry models used are shown in Supplementary

Fig. 3. For a given voltage between the emitter and the anode plate, the electrostatic field distribution over the emitter-shape-model surface is first calculated by finite-element methods (FEM), where the FEFs γ_a can also be obtained. Then, the total predicted emission current is obtained by integration of local emission current density (LECD) over the shape-model surface, using the planar emission approximation and the MG FE equation (see Supplementary Note 1 and Supplementary Eq. (S2)). The planar emission approximation assumes that the LECD J_L at any particular location "L" on the emitter surface is given by some specified planar emission equation, using the values at "L" of the local work function and the surface electrostatic field magnitude[34]. For a specific model and emission current, we find that theoretically predicted voltage values V_{MG} are less than those V_m found experimentally for the same gap spacing d. This suggests that (other things being equal) MG FE theory may be over-predicting LECDs. To quantify the discrepancy, we introduced a correction factor $C_{MG} < 1$. Specifically, due to the consistent scaling relationship at different currents ($I_m = 2$ nA, 10 nA, 50 nA, and 100 nA) as shown in Fig. 1 and Supplementary Fig. 4, we selected the voltage at $I = 2$ nA to calculate C_{MG}, ($C_{MG} = [V_{MG}(I_{MG} = 2 \text{ nA})]/[V_m(I_m = 2 \text{ nA})]$), then the effective voltage for all V_{MG} values can be expressed as: $V_{MG\text{-eff}} = V_{MG}/C_{MG} \approx V_m$. The theoretical I_{MG}-$V_{MG\text{-eff}}$ curves and corresponding theoretical FN plots obtained are shown in Fig. 2a, b (dotted lines), which are closely aligned with the experimental data. Figure 4a illustrates the numerical values of correction factors C_{MG} as a function of R/d in logarithmic coordinates. As R/d increases, C_{MG} initially increases from approximately 0.4 and gradually approaches 0.7. This confirms experimentally the discrepancies between the actual field emission and theoretical predictions[64].

Figure 4b, c show the effective field-voltage conversion factors $\beta_{\text{eff-MG}}$ ($\beta_{\text{eff-MG}} = C_{MG}\beta_a = C_{MG}\gamma_a/d$) and shape factors k_{MG} ($\beta_{\text{eff-MG}} = 1/(k_{MG}R)$) as functions of R/d in logarithmic coordinates. The relationships $\beta_{\text{eff-MG}} \propto (R/d)^{n_4}$ and $k_{MG} \propto (R/d)^{-n_5}$ are used to fit n_4 and n_5. For $R/d < 0.1$, n_4 increases slowly to about 0.2, rises rapidly to 0.9 as R/d approaches 10, and then increases more slowly towards 1 for $R/d > 10$, following $\beta_{\text{eff-MG}} \propto R/d$ (Fig. 4b). This is consistent with the n_1 trend reported in Fig. 2c. Surprisingly, the scaling of k_{MG} is valid for all tungsten nanotips with different R, which converges onto a single line with R/d (Fig. 4c). Analogously, for R/d values less than 0.1, n_5 rises slowly to about 0.2, increases rapidly to 0.9 as R/d approaches 10, and then rises more slowly towards 1 for $R/d > 10$, following $k_{MG} \propto d/R$ (for planar geometry) and indicating a nearly uniform electrostatic field distribution between the emitter apex and the anode plane. As we can see, the k_{MG} values ranging from 0.02 to 4 provide a clear and detailed characterization of field emission of a nanotip in a nanogap. We believe that these scaling laws should be valid for any metallic nanotip of apex radius R in a nanogap of spacing d, in the range of $R/d = 0.04$ to 48
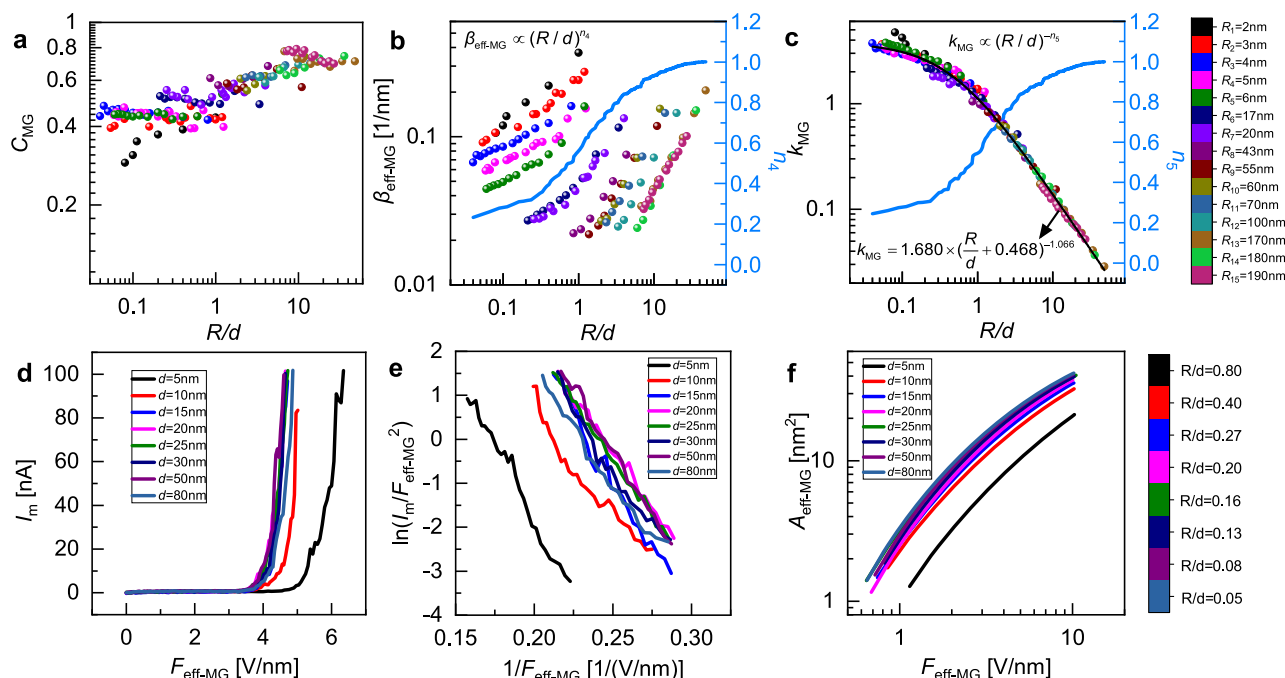
Fig. 4 | The geometric effects in nanoscale field emission. a The correction factors C_{MG} as a function of the ratio of apex radius to gap length R/d in logarithmic coordinates (scatterplots). **b** The effective field-voltage conversion factors $\beta_{eff\text{-}MG}$ as a function of R/d in logarithmic coordinates (scatterplots), along with the corresponding exponent n_4 (solid line). **c** The shape factors k_{MG} as a function of R/d in logarithmic coordinates (scatterplots), along with the corresponding negative exponent n_5 (solid line). The black line shows the fitting curve by $k_{MG} = 1.680 \times (R/d)^{-1.066}$. **d** The field emission I_m-$F_{eff\text{-}MG}$ curves of the tungsten nanotip with an apex radius of 4 nm across different nanogaps. **e** The corresponding Fowler-Nordheim (FN) plots of I_m-$F_{eff\text{-}MG}$ curves. **f** The effective emission area $A_{eff\text{-}MG}$ obtained by finite element method (FEM) simulation.

reported experimentally in this work. For the ease of applications, the values of k_{MG} can be fitted into a simple analytical expression depending of R/d, which is $k_{MG} = 1.680 \times (R/d + 0.468)^{-1.066}$ (based on Fig. 4c, with a R-squared fitting of 0.986). Thus, the electrostatic field F in the MG FE equation (Supplementary Eq. (S2)) should be substituted by the effective electrostatic field $F_{eff\text{-}MG}$

$$F_{eff-MG} = \beta_{eff-MG} V_m = C_{MG}\beta_a V_m = C_{MG}\gamma_a V_m/d = C_{MG}\gamma_a F_G = V_m/(k_{MG}R) \quad (1)$$

where $F_{eff\text{-}MG}$ is the effective apex-field. Then, the total field emission current can be estimated by

$$I_m = A_{eff-MG} J_{eff-MG} = A_{eff-MG} a\phi^{-1} F_{eff-MG}^2 t^{-2}(y) \exp\left[-\frac{v(y)b\phi^{3/2}}{F_{eff-MG}}\right] \quad (2)$$

where $J_{eff\text{-}MG}$ is the effective apex emission current density, $A_{eff\text{-}MG}$ is effective emission area, a ($= 1.54 \times 10^{-6}$ [A eV V^{-2}]) and b ($= 6.83$ [eV$^{-3/2}$ V nm^{-1}]) are constants, y is the Nordheim parameter (where $y = (1.20$ eV V$^{-1/2}$ nm$^{1/2})$ $F^{1/2}/\phi$, and F is in V/nm), and $t(y)$ and $v(y)$ are well-known mathematical functions[26–28].

Based on the proposed equation, the applied voltage V_m in field emission characteristics of the tungsten nanotip with a radius of curvature of 4 nm shown in Fig. 2a, b can be replaced by the effective apex-field, $F_{eff\text{-}MG}$. Figure 4d, e show the field emission I_m-$F_{eff\text{-}MG}$ curves and their corresponding FN plots. Notably, as d increases, the I_m-$F_{eff\text{-}MG}$ curves gradually converge for $R/d \leq 0.27$. The observed differences in the curves at $d = 5$ nm ($R/d = 0.8$) and $d = 10$ nm ($R/d = 0.4$) can be explained by the effective emission area $A_{eff\text{-}MG}$ in Fig. 4f. As the gap increases with $R/d \leq 0.27$, the effective emission area increases and converges gradually. However, for $d = 5$ nm ($R/d = 0.8$), especially or $d = 10$ nm ($R/d = 0.4$), the effective emission area remains below this convergent value, indicating that the nanotip requires a higher electrostatic field to maintain the same field emission current I_m. This

causes the deviations of the I_m-$F_{eff\text{-}MG}$ curves and the corresponding FN plots when $R/d > 0.27$, differing from the reported collapsing $\log_{10}(I/F^2)$ - $1/F$ curves in ref. 65, where the change of emission area is not considered. Despite this difference at $R/d > 0.27$, the collapsing I-V curves and the FN plots reported in ref. 65 are consistent with our findings for $R/d < 0.27$. To be specific, the I-V curves can collapse onto one single I-$VR(d)$ curve, with $R(d)$ approximating a power law $R(d) \propto d^{-\lambda}$ (where $\lambda \approx 0.22$ for $d = 3$–300 nm and $R \approx 5$ nm). Furthermore, they found that when $d > 10$ nm, $V \propto d^\lambda$ with $\lambda \approx 0.2$–0.35, while λ towards to a larger value for $d < 10$ nm[65]. This well matches our universal scaling $V_m \propto d^{n_1}$ for a nanotip with R as the radius of curvature, where n_1 increases slowly at approximately 0.2 for $R/d < 0.1$, which proves the validity of our proposed models for field emission of nanotip in nanogap as studied in this work.

Based on the above analysis, the effects of the emitter's non-planar shape are more important for $R/d = 0.04$ to 48 as studied in our experiment. Therefore, we utilize the Kyritsakis-Xanthakis (KX) FE equation[42], including surface curvature corrections for local electrostatic potential and the image charge potential which is valid only along the emitter's axis (see Supplementary Note 1 and Supplementary Eq. (S4)), to derive the correction factor C_{KX}, effective field-voltage conversion factors $\beta_{eff\text{-}KX}$ and k_{KX} as functions of R/d, along with the corresponding power exponents, as provided in Supplementary Note 4 and Supplementary Fig. 6. This approach, based on the planar emission approximation, is similar to the process used for deriving C_{MG}, $\beta_{eff\text{-}MG}$ and k_{MG}. As shown in Supplementary Fig. 6, for $R/d < 1$, C_{KX} is greater than C_{MG}, increasing from 0.5 (whereas C_{MG} increases from 0.4 in Fig. 4a), due to the inclusion of the curvature correction effects. For $R/d > 1$, C_{KX} is consistent with C_{MG}, and approaches 0.7. Therefore, despite these corrections, the KX FE equation (ref. 42), which uses an Earthed-sphere model to assess surface curvature effects, still does not accurately predict the field emission current of nanotips.

Interestingly, the investigation of electron tunneling process between the planar substrate and the non-planar tips (spherical or hyperboloidal geometry) decades ago has already concluded that electron field emission current density in a nanogap is significantly regulated by the two factors including the asymmetry in the geometries of cathode and anode, and the overall image charge potential of space charge with both electrodes. Those effects on the overall image charge potential have been carefully examined in refs. 29,30 for sphere-plane electrode configuration with nanogaps using the rigorous electrodynamic models under spherical and prolate spheroidal coordinates. It was found that the non-planar geometry of cathode could directly result in the anisotropic distribution of image charge potential spatially surrounding the cathode. Most importantly, the overall image charge potential of sphere-plane system in nanogap was predicted to be less negative near the cathode, compared to that of plane-plane configuration, indicating an increasing of electron transmission barrier height in the former case due to the anticipated geometric asymmetry in electrode pair. Furthermore, the increasing of geometric asymmetry further diminishes the lowering of electron emission barrier height, because the complete multiple-image potential goes to less negative, relative to that of plane-plane geometry. For example, using the exact image charge potential model given in ref. 30 for hyperboloidal tip model (tungsten electrode with $R = 10$ nm and $d = 1$, 2, and 3 nm, respectively), for $R/d = 10$, 5.0, and 3.3, the absolute values are reduced by 1.0%, 1.9%, and 2.9%, compared to those of plane-plane system, respectively. The raising of electron transmission energy barrier height with the increasing of the geometric asymmetry in nanogap for anode-cathode system can reduce the emission current density in comparison with that of plane-plane configuration under the same electrostatic field. This may be the main reason for the presence of the correction factor $V_{MG} = C_{MG}V_m < V_m$ between experimental field emission curves and the MG FE equation, as shown in Fig. 4a. These insight inspires further theoretical exploration to refine predictions for nanoscale field emission phenomena, where the three-dimensional image charge potential between space charges and the bulk charges in the both electrodes (anode and cathode) should be especially considered[30].

In this study, we delved into the experimental relationship between field emission characteristics of nanotips in nanogaps and the ratio of apex radius to gap length (R/d). We demonstrated that space charge quantum effects are not considerable in the range of $R/d = 0.04$ to 48, while the effects of quantum tunnelling due to the emitter shape are predominant. Based on our experimental results, we proposed a modified field emission (FE) equation, where the effective electrostatic field at the emitter apex is given by $F_{eff-MG} = V_m/(k_{MG}R)$, with a detailed analytical expression for the shape factor, $k_{MG} = 1.680 \times (R/d + 0.468)^{-1.066}$. These findings are believed to be valid for any metallic nanotip in the range of $R/d = 0.04$ to 48. It is important to note that despite the success and limitation of 1D field emission models (many different versions), all models require some approximation to derive some scaling laws or equations to compare with experimental results. Physics-consistent 3D model for arbitrary shape of emitter is likely to be impossible. In this paper, we performed a clear measurement of field emission from an emitter of radius $R = 2$ to 190 nm in a nanogap of $d = 5$ nm to 100 nm and provide a first experimental-proved scaling that is valid over a wide range of R/d (4 order of magnitude). Discussion of this scaling to other models can be referred to Supplementary Note 4. Our work underscores the importance of emitter shape effects in dictating the emission properties, and highlights the need for precise theoretical models to accurately predict and harness these effects in practical applications, which is crucial for understanding and improving the performance of nanoelectronic devices.

Methods

In situ electrical experiment system

The in situ electrical experiment system consists of the transmission electron microscopy (JEOL-2100F TEM) and an in situ electrically biased TEM holder (ZepTools Technology). This setup achieves a spatial resolution of 0.1 nm and allows for nanogap adjustment with an accuracy of 0.04 nm. During field emission measurements, the system can apply a direct current voltage of up to 150 V across nanogaps, with a current measurement resolution of 0.1 nA. The in situ electrically biased TEM holder and the schematic diagram of the field emission measurement are shown in Supplementary Fig. 1a, b. All measurements are performed at room temperature and a vacuum level of ~10^{-5} Pa.

Fabrication of the pure tungsten nanotips

The preparation of the tungsten nanotips involves two steps. The first step is an ex-situ double-electrolyte electrochemical etching method[57,58], and the schematic is shown in Supplementary Fig. 1c. Specifically, a stepping motor (TSTA-1050, 7-star, Beijing) precisely controls the motion of a 99.97% pure tungsten wire with a diameter of 0.3 mm. The tungsten wire passes through a 5 M NaOH electrolyte lamella (flake, purity 97%, Aladdin) and is immersed perpendicularly in a saturated NaCl solution (AR, Aladdin). A DC power source (B2091A, Keysight, USA) supplies a voltage of 5 V to a stainless-steel anode immersed in the saturated NaCl solution and a ring inert nickel-chromium cathode (diameter 10 mm). The tungsten wire is etched only in the NaOH lamella, with the NaCl solution acting as a conducting element between the tungsten wire and the stainless-steel anode. Once the tungsten wire breaks, the electric circuit is automatically cut off as the lower fragment of the tungsten wire drops. However, although the apex radius of the prepared tungsten nanotip by first step is less than 50 nm, there is an unavoidable oxide layer with a few nanometers thick on the tungsten nanoelectrode surface due to the ex-situ preparation, which significantly affects the field emission characteristics.

The second step is an in situ Joule melting method. Initially, the tungsten nanoelectrodes prepared by the first step and the gold plate (prepared by pressing and cutting) are mounted on the TEM electrical sample holder, as shown in Supplementary Fig. 1a. Next, the inter-electrode gap is adjusted in situ to less than 20 nm under TEM. A ramped DC voltage is then applied across the nanogap to induce electrical breakdown, with the tungsten nanotip acting as the cathode and the gold plate as the anode. Following the breakdown, the tungsten nanotips with radii of curvature from 2 nm to 200 nm can be prepared in situ. The surfaces of the tungsten nanotips prepared by this method are very clean and free of contaminants such as oxide layer. This is demonstrated by the representative high-resolution TEM images and the selected area electron diffraction results of the pure tungsten nanotip with an apex radius of 5 nm, as shown in Supplementary Fig. 1d.

Finite element method (FEM) numerical simulations

The FEFs are obtained using a commercial FEM tool (COMSOL Multiphysics). First, the sphere-on-cone nanotip models are established based on the morphology of all the tungsten nanotips shown in Fig. 1. Material parameters are based on the default values provided by the COMSOL internal library. It's worth noting that the heights of practical tungsten nanotips are approximately 1 cm, i.e., $H_m \gg R_m$ and $H_m \gg d_m$ (in a near anode configuration), and in order to reduce the effect of the simulated heights on the simulated electrostatic fields, we set the height of the simulated models at $H_t/R_t = 400$. The reason is that according to the Supplementary Fig. 2, when H_t/R_t is greater than 400, the selected heights have little effect on the FEF, given that the minimum R_t/d_t ratio in our experiments is 0.04. Next, the electrostatic fields are simulated using the electrostatics module. The FEF γ_a can be obtained as $\gamma_a = F_a/F_G$, where F_a represents the electrostatic surface-

field magnitude at the emitter apex, and F_G is the average field amplitude in the gap between the emitter apex and the anode plate, given by $F_G = V/d$. Then, the total predicted emission current is obtained by integration of LECD over the shape-model surface, using the planar emission approximation and the MG FE equation[26–28] or KX FE equation[42] (see Supplementary Note 1 and Supplementary Eqs. (S2) and (S4)). The planar emission approximation assumes that the LECD J_L at any particular location "L" on the emitter surface is given by some specified planar emission equation, using the values at "L" of the local work function and the surface electrostatic field magnitude[34]. Supplementary Fig. 3 shows the electrostatic field distribution, as well as field emission current density J_{MG} and J_{KX} (two-dimensional linear current density) for the nanotip with an apex radius of 4 nm at $d = 5$ nm and $V = 20$ V.

Data availability

The authors declare that all relevant data supporting the findings of this work are included in the Article, with additional data provided in the Supplementary Information. Source data are provided with this paper.

References

1. Hernandez, N. et al. Field emission characteristics of AlGaN/GaN nanoscale lateral vacuum diodes. *J. Appl. Phys.* **135**, 204305 (2024).
2. Xu, J. et al. High-quality and stable electron emission device with sub-30-nm aligned nanogap arrays. *IEEE Trans. Electron Devices* **64**, 2364–2368 (2017).
3. Brimley, S., Miller, M. S. & Hagmann, M. J. Field emission in air and space-charge-limited currents from iridium-iridium oxide tips with gaps below 100 nm. *J. Appl. Phys.* **109**, 094510 (2011).
4. Srisonphan, S. Nanogaps mediated field effect-controlled field emission triode. *Acs Appl. Electron. Mater.* **4**, 4857–4862 (2022).
5. Srisonphan, S. Field effect-controlled space-charge limited emission triode with nanogap channels. *IEEE Electron Device Lett.* **42**, 1540–1543 (2021).
6. Pescini, L. et al. Nanoscale lateral field-emission triode operating at atmospheric pressure. *Adv. Mater.* **13**, 1780–1783 (2001).
7. Nguyen, H. D., Kang, J. S., Li, M. & Hu, Y. J. High-performance field emission based on nanostructured tin selenide for nanoscale vacuum transistors. *Nanoscale* **11**, 3129–3137 (2019).
8. Srisonphan, S., Jung, Y. S. & Kim, H. K. Metal-oxide-semiconductor field-effect transistor with a vacuum channel. *Nat. Nanotechnol.* **7**, 504–508 (2012).
9. Han, J. W., Seol, M. L., Kim, J. & Meyyappan, M. Nanoscale complementary vacuum field emission transistor. *ACS Appl. Nano Mater.* **3**, 11481–11488 (2020).
10. Han, J. W., Seol, M. L., Moon, D. I., Hunter, G. & Meyyappan, M. Nanoscale vacuum channel transistors fabricated on silicon carbide wafers. *Nat. Electron* **2**, 405–411 (2019).
11. Nirantar, S. et al. Metal-air transistors: semiconductor-free field-emission air-channel nanoelectronics. *Nano Lett.* **18**, 7478–7484 (2018).
12. Chang, W. T. & Pao, P. H. Field electrons intercepted by coplanar gates in nanoscale air channel. *IEEE Trans. Electron Devices* **66**, 3961–3966 (2019).
13. Nikoo, M. S. & Matioli, E. Electronic metadevices for terahertz applications. *Nature* **614**, 451–455 (2023).
14. Nikoo, M. S. et al. Nanoplasma-enabled picosecond switches for ultrafast electronics. *Nature* **579**, 534–539 (2020).
15. Xu, J., Wang, Q. L., Qi, Z. Y., Zhai, Y. S. & Zhang, X. B. Study on the frequency characteristics of nanogap electron devices. *J. Appl. Phys.* **117**, 204504 (2015).
16. Loganathan, K. et al. Rapid and up-scalable manufacturing of gigahertz nanogap diodes. *Nat. Commun.* **13**, 3260 (2022).
17. Li, N. N., Zhang, B. L., He, Y. & Luo, Y. Sub-picosecond nanodiodes for low-power ultrafast electronics. *Adv. Mater.* **33**, 2100874 (2021).
18. Zhang, H. J. et al. Polymer-protected sub-2-nm-nanogap fabrication for biological sensing in near-physiological conditions. *Small* **5**, 2797–2801 (2009).
19. Ivanov, A. P. et al. DNA tunneling detector embedded in a nanopore. *Nano Lett.* **11**, 279–285 (2011).
20. Chen, X. et al. Electrical nanogap devices for biosensing. *Mater. Today* **13**, 28–41 (2010).
21. Xiang, D., Jeong, H., Lee, T. & Mayer, D. Mechanically controllable break junctions for molecular electronics. *Adv. Mater.* **25**, 4845–4867 (2013).
22. Durkan, C. & Zhang, Q. Towards reproducible, scalable lateral molecular electronic devices. *Appl. Phys. Lett.* **105**, 083504 (2014).
23. Han, J. W., Oh, J. S. & Meyyappan, M. Vacuum nanoelectronics: back to the future?-Gate insulated nanoscale vacuum channel transistor. *Appl. Phys. Lett.* **100**, 213505 (2012).
24. Han, J. W., Moon, D. I. & Meyyappan, M. Nanoscale vacuum channel transistor. *Nano Lett.* **17**, 2146–2151 (2017).
25. Li, X. H. & Feng, J. J. Review of nanoscale vacuum devices. *Electron.-Switz.* **12**, 802 (2023).
26. Murphy, E. L. & Good, R. H. Thermionic emission, field emission, and the transition region. *Phys. Rev.* **102**, 1464–1473 (1956).
27. Egorov, N. & Sheshin, E. *Field Emission Electronics* (Springer, Cham, 2017).
28. Fursey, G. N. *Field Emission in Vacuum Microelectronics* (Springer, New York, 2005).
29. Morawitz, H., Batra, I. P., Reinisch, R. & Henry, G. R. Multiple image potential effects in a simple-model of the scanning tunneling microscope (STM). *Surf. Sci.* **180**, 333–352 (1987).
30. Miskovsky, N., Cutler, P., Feuchtwang, T. & Lucas, A. A Green's function solution to the image and multiple image interactions for hyperboloidal geometry: application to metallic pointcontact infrared detectors. *Int. J. Infrared Millim. Waves* **2**, 739–772 (1981).
31. Zhang, P., Valfells, A., Ang, L. K., Luginsland, J. W. & Lau, Y. Y. 100 years of the physics of diodes. *Appl. Phys. Rev.* **4**, 011304 (2017).
32. Li, Y. M. et al. Review of electron emission and electrical breakdown in nanogaps. *Phys. Plasmas* **31**, 040502 (2024).
33. Zhang, P. et al. Space-charge limited current in nanodiodes: ballistic, collisional, and dynamical effects. *J. Appl. Phys.* **129**, 100902 (2021).
34. de Assis, T. A., Dall'Agnol, F. F. & Forbes, R. G. Field emitter electrostatics: a review with special emphasis on modern high-precision finite-element modelling. *J. Phys.-Condens Mat.* **34**, 493001 (2022).
35. Gaertner, G., Knapp, W. & Forbes, R. G. *Modern Developments in Vacuum Electron Sources Preface* (Springer, Cham, 2020).
36. Cutler, P. H., He, J., Miskovsky, N. M., Sullivan, T. E. & Weiss, B. Theory of electron-emission in high fields from atomically sharp emitters - Validity of the Fowler-Nordheim equation. *J. Vac. Sci. Technol. B* **11**, 387–391 (1993).
37. Fursey, G. N. & Glazanov, D. V. Deviations from the Fowler-Nordheim theory and peculiarities of field electron emission from small-scale objects. *J. Vac. Sci. Technol. B* **16**, 910–915 (1998).
38. He, J. et al. Derivation of the image interaction for non-planar pointed emitter geometries: application to field emission I–V characteristics. *Surf. Sci.* **246**, 348–364 (1991).
39. Biswas, D. & Ramachandran, R. The image-charge correction for curved field emitters (vol 24, 073107, 2017). *Phys. Plasmas* **24**, 079901 (2017).
40. Jensen, K. L., Shiffler, D. A., Harris, J. R., Rittersdorf, I. M. & Petillo, J. J. 2D/3D image charge for modeling field emission. *J. Vac. Sci. Technol. B* **35**, 02C101 (2017).
41. Kyritsakis, A., Xanthakis, J. P. & Pescia, D. Scaling properties of a non-Fowler-Nordheim tunnelling junction. *P. R. Soc. a-Math. Phy.* **470**, 20130795 (2014).

42. Kyritsakis, A. & Xanthakis, J. P. Derivation of a generalized Fowler-Nordheim equation for nanoscopic field-emitters. *P. R. Soc. a-Math. Phy* **471**, 20140811 (2015).

43. Jensen, K. L., Shiffler, D. A., Peckerar, M., Harris, J. R. & Petillo, J. J. Current from a nano-gap hyperbolic diode using shape-factors: theory. *J. Appl Phys.* **122**, 064501 (2017).

44. Binh, V. T., Purcell, S., Garcia, N. & Doglioni, J. Field-emission electron spectroscopy of single-atom tips. *Phys. Rev. Lett.* **69**, 2527 (1992).

45. Purcell, S. T. et al. Field-emission from narrow bands above the Fermi-level of nanometer-scale objects. *Phys. Rev. B* **49**, 17259–17263 (1994).

46. Patterson, A. A. & Akinwande, A. I. Elementary framework for cold field emission: Incorporation of quantum-confinement effects. *J. Appl. Phys.* **114**, 234303 (2013).

47. Kleshch, V. I., Zestanakis, P. A. & Xanthakis, J. P. Breakdown of plane-wave-based theories of field emission from a subnanometer-radius tip. *Appl. Surf. Sci.* **623**, 156990 (2023).

48. Chatziafratis, A. & Xanthakis, J. P. Field emission from a nanometric paraboloidal emitter. *J. Electron Spectrosc. Relat. Phenom.* **241**, 146871 (2020).

49. Chatziafratis, A., Fikioris, G. & Xanthakis, J. P. Exact eigenstates of a nanometric paraboloidal emitter and field emission quantities. *P. R. Soc. a-Math. Phy* **474**, 20170692 (2018).

50. Banerjee, S. & Zhang, P. A generalized self-consistent model for quantum tunneling current in dissimilar metal-insulator-metal junction. *AIP Adv.* **9**, 085302 (2019).

51. Zhang, P. Scaling for quantum tunneling current in nano- and subnano-scale plasmonic junctions. *Sci. Rep.* **5**, 09826 (2015).

52. Zhang, P. & Lau, Y. Y. Ultrafast and nanoscale diodes. *J. Plasma Phys.* **82**, 595820505 (2016).

53. Koh, W. S. & Ang, L. K. Quantum model of space-charge-limited field emission in a nanogap. *Nanotechnology* **19**, 235402 (2008).

54. Li, N., Wu, K., Cheng, Y. H. & Xiao, B. Self-consistent numerical solution of quantum regime with exchange-correlation effects of space charges for electron field emission in a nano-gap. *Front. Phys.* **11**, 1223704 (2023).

55. Meng, G. et al. In situ Observation of Field-induced nanoprotrusion growth on a carbon-coated tungsten nanotip. *Phys. Rev. Lett.* **132**, 176201 (2024).

56. Li, Y., Zhan, F., Tang, J., Cheng, Y. & Meng, G. Effect of cathode radius on the pre-breakdown characteristics in vacuum nanogaps. In *30th International Symposium on Discharges and Electrical Insulation in Vacuum (ISDEIV).* (ed. Motoyoshi, T.) 1–4 (Institute of Electrical and Electronics Engineers (IEEE), 2023).

57. Li, Y. Z. et al. A double-electrolyte etching method of high-quality tungsten probe for undergraduate scanning tunneling microscopy and atomic force microscopy experiments. *Eur. J. Phys.* **40**, 025004 (2019).

58. Li, B. W. et al. Fabricating ultra-sharp tungsten STM tips with high yield: double-electrolyte etching method and machine learning. *Sn Appl. Sci.* **2**, 1246 (2020).

59. Meng, G. D., Cheng, Y. H., Wu, K. & Chen, L. Electrical characteristics of nanometer gaps in vacuum under direct voltage. *IEEE Trans. Dielectr. Electr. Insul.* **21**, 1950–1956 (2014).

60. Zuber, J. D., Jensen, K. L. & Sullivan, T. E. An analytical solution for microtip field emission current and effective emission area. *J. Appl. Phys.* **91**, 9379–9384 (2002).

61. Jensen, K. L. Exchange-correlation, dipole, and image charge potentials for electron sources: Temperature and field variation of the barrier height. *J. Appl. Phys.* **85**, 2667–2680 (1999).

62. Child, C. D. Discharge from hot CaO. *Phys. Rev.* **32**, 0492–0511 (1911).

63. Langmuir, I. The effect of space charge and residual gases on thermionic currents in high vacuum. *Phys. Rev.* **2**, 450–486 (1913).

64. Forbes, R. G. Development of a simple quantitative test for lack of field emission orthodoxy. *Proc. R. Soc. A: Math., Phys. Eng. Sci.* **469**, 20130271 (2013).

65. Cabrera, H. et al. Scale invariance of a diodelike tunnel junction. *Phys. Rev. B* **87**, 115436 (2013).

Acknowledgements

Author contributions

G.M., Y.C., and Y.L. conceived the project. L.K.A. contributed expertise and assistance in theoretical guidance. B.X. contributed expertise and assistance in simulation guidance. Y.L. carried out the experiments and simulations, analyzed the data, and wrote the original manuscript. L.X., S.T., Y.G., and J.W. assisted with experimentation. N.L. assisted with simulations. All authors contributed to the discussion of the data and to writing the manuscript. All authors have given approval to the final version of the manuscript.

Competing interests

The authors declare no competing interests.

Additional information

Supplementary information The online version contains supplementary material available at https://doi.org/10.1038/s41467-025-60607-6.

Correspondence and requests for materials should be addressed to Lay Kee Ang or Guodong Meng.

Peer review information *Nature Communications* thanks John P. Xanthakis, and the other, anonymous, reviewer(s) for their contribution to the peer review of this work. A peer review file is available.

Reprints and permissions information is available at http://www.nature.com/reprints

Publisher's note Springer Nature remains neutral with regard to jurisdictional claims in published maps and institutional affiliations.